Quantum modulation of a coherent state with a single electron spin

P. Androvitsaneas,[1,2,*] A. B. Young,[2,*] T. Nutz,[2] J. M. Lennon,[2] S. Mister,[2] C. Schneider,[3] M. Kamp,[4] S. Höfling,[4] D. P. S. McCutcheon,[2] E. Harbord,[2] J. G. Rarity,[2] and R. Oulton[2]

[1]*School of Engineering, Cardiff University, Queen's Building, The Parade, Cardiff, CF24 3AA, United Kingdom*
[2]*QETLabs, H. H. Wills Physics Laboratory, University of Bristol, Tyndall Avenue, Bristol, BS8 1TL, United Kingdom, and Department of Electrical & Electronic Engineering, University of Bristol, BS8 1FD, United Kingdom*
[3]*Institute of Physics, University of Oldenburg, D-26129 Oldenburg, Germany*
[4]*Technische Physik, Physikalisches Institut and Wilhelm Conrad Röntgen-Center for Complex Material Systems, Universität Würzburg, Am Hubland, 97474 Würzburg, Germany*

(Received 19 July 2022; accepted 7 February 2024; published 14 June 2024)

The interaction of quantum objects lies at the heart of fundamental quantum physics and is key to a wide range of quantum information technologies. Photon-quantum-emitter interactions are among the most widely studied. Two-qubit interactions are generally simplified into two quantum objects in static well-defined states. In this work we explore a fundamentally new dynamic type of spin-photon interaction. We demonstrate the modulation of a coherent narrowband laser by a coherently evolving spin in the ground state of a quantum dot. What results is a quantum modulation of the output phase (either 0 or π but no values in between), and a new quantum state of light that cannot be described classically.

DOI: 10.1103/PhysRevResearch.6.023276

The resonantly scattered field (RSF) from a two-level system has been extensively studied over the past 50 years [1–5], and it is considered a well understood phenomenon in physics that underpins a range of quantum technologies [6–9]. The coherent fraction of the resonantly scattered field retains the bandwidth of the driving laser but becomes antibunched on the timescale of the incoherent fraction (assuming sufficient detector bandwidth) [5,10–12]. Less explored is how the RSF is altered if the quantum emitter contains a ground-state spin. For a high magnetic field the system splits into spectrally distinct transitions that can be probed individually, where it has been shown that the RSF either retains the coherence of the drive field or undergoes dephasing on the same timescale as the electron spin $T_2{}^*$ time [13]. The RSF from a optically active spin is generally simplified into separate uncoupled two-level systems [8,14–16]. However, in the low magnetic field limit where the Zeeman splitting ($2\omega_B$) is less than the natural line-width of the optical transitions (Γ), the complex interplay between all overlapping transitions must be taken into account.

In this limit we reveal that the RSF does not adopt any of the previously observed behaviours (except antibunching), but rather the spin imparts a quantum phase modulation to the RSF. Our previous RSF studies of efficient QD spin micropillar systems in high magnetic field have shown that a phase shift is imparted on the RSF [17,18]. Since the charged QD has circularly polarized transitions [Fig. 1(a)] this phase shift can be used to rotate linearly polarized light [17–23]. In the following we consider a narrowband single-photon state in the weak excitation limit (i.e., no exciton creation). As we have discussed in previous work [17,18] horizontally polarized (H) single photons will scatter from the charged QD and undergo a Faraday rotation towards vertical (V) due to the circularly polarized selection rules [each spin $|\uparrow_z\rangle$, $|\downarrow_z\rangle$ interacts only with one circular component see Fig. 1(a)]. The cross-polarized output field will depend on the spin oreintation and is given by

$$\begin{aligned} |\psi\rangle_{\text{in}} = |\uparrow\rangle_z|H\rangle \rightarrow |\psi\rangle_{\text{out}} = |\uparrow\rangle_z|V\rangle, \\ |\psi\rangle_{\text{in}} = |\downarrow\rangle_z|H\rangle \rightarrow |\psi\rangle_{\text{out}} = -|\downarrow\rangle_z|V\rangle \end{aligned} \tag{1}$$

(see Appendix A and Ref. [14] for details). This expression is true in the limit of a perfect cavity, where a deterministic perfect rotation to the orthogonal state is possible. Any deviation from that results only in a reduction of efficiency, as any light remaining in the same polarization as the laser has no back-action on the spin state. States $|\uparrow/\downarrow\rangle_z$ represent spin orientations along the growth (optical) axis of the QD. The input photon is perfectly rotated to V polarization with a global phase shift 0 or π depending on the spin state. Both spin states rotate the polarization to vertical (V) but take orthogonal trajectories (clockwise/anticlockwise) around the Poincaré sphere, giving rise to a global phase difference. The global phase arises from the intrinsic phase difference of the σ^+ and σ^- components of linearly polarized light, imprinted by the circularly polarized optical transitions of the spin [Fig. 1(a)].

*These authors contributed equally to this work.

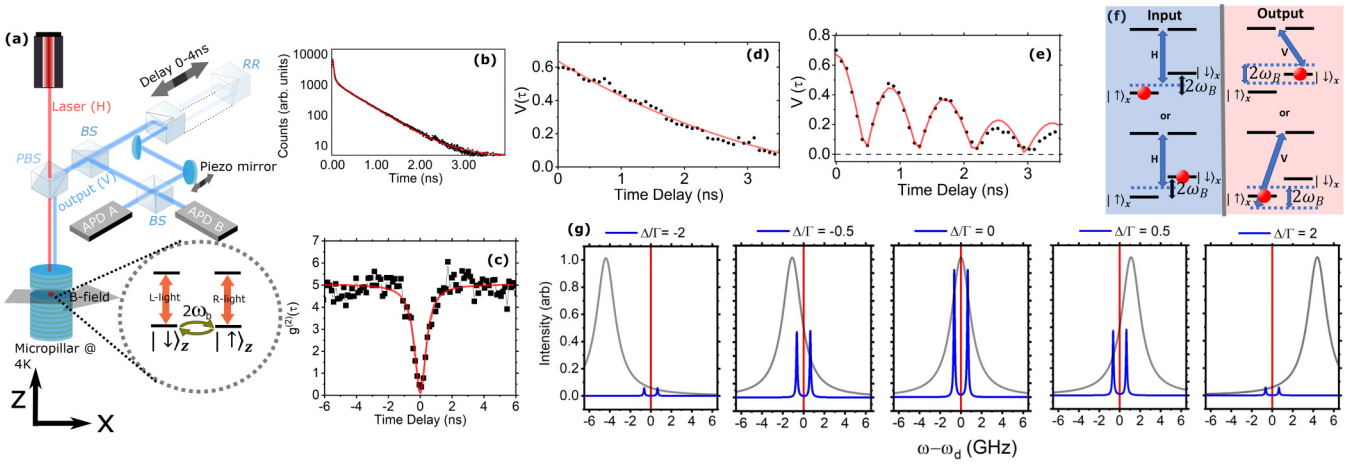

FIG. 1. Experimental setup for probing the RSF a QD spin (QD1) in a pillar microcavity showing the optical selection rules for the spin in the $|\uparrow/\downarrow\rangle_z$ basis in a weak in-plane (Voigt) magnetic field which induces Larmor precession at frequency $2\omega_B$. In our experiment the drive field is a horizontally polarized (H) single-frequency laser (along x). A polarizing beam splitter (PBS) separates the H polarized pump from the V polarized signal. The output signal is split on a 50:50 beam splitter (BS) which forms the two arms of a MZI. (b) Spontaneous emission lifetime measurements obtained via pulsed resonant excitation (2 ps) for QD1 where $T_1 = 460 \pm 6$ ps, corresponding to a transform limited line-width of $\Delta\omega \sim 1.3$ μeV. The initial fast decay is a result of background light from the pulsed drive laser with a timing response limited by the detector jitter (∼64 ps). (c) Antibunching $g_2(t)$ measurement of the RSF using a Hanbury Brown-Twiss experiment. Here we observe a pronounced antibunching feature with the width determined by the excited trion state lifetime. The pronounced bunching outside of the dip arises due to spectral jitter (d), (e) Plots showing the visibility $[V(\tau)]$ of the RSF as measured with the MZI in panel (a) for (d) $B = 0$, and (e) $B = 108$mT, for a drive-field laser power $P \sim 0.02P_{\text{sat}}$. The oscillations in panel (e) are at a frequency of $2\omega_B = 590 \pm 10$ MHz, as a result of Larmor precession and represents a subnatural line-width Zeeman splitting ∼0.4 μeV. (f) An illustration of the resonant scattering process in the $|\uparrow/\downarrow\rangle_x$ basis which represent eigenstates of the spin along the direction of the applied magnetic field, separated in energy by $2\omega_B$. Since $2\omega_B < \Gamma$ this forms a coupled pair of Λ systems where spin preserving optical transitions are H-polarized and spin flipping transitions are V-polarized. (g) Fourier transforms of spectra calculated using parameters from panel (e) and using a master equation based on the level system in panel (f), where every V-polarized photon that is scattered is a result of a spin flip in the $|\uparrow/\downarrow\rangle_x$ basis which to conserve energy results in an energy shifted scattered photon. The gray line represents a Lorentzian with a bandwidth corresponding to Γ to emphasise the subnatural linewidth splitting of the RSF spectrum. Each individual panel shows how the RSF spectra varies with QD-laser detuning Δ and the red line the single-frequency CW drive laser.

One rarely needs to consider this global phase, but an interesting situation arises when the spin evolves coherently in an in-plane (Voigt) magnetic field B_x with a relatively slow Larmor precession period ($2\omega_B < \Gamma$, where Γ is the radiative lifetime of the optical transitions). To probe these dynamics we measure the first-order correlation function $g^{(1)}(t)$ of the RSF. The correlation function is measured using a Mach Zehnder interferometer [Fig. 1(a)] which measures the self-interference of the RSF by splitting it into two beams and interfering the signal at time $t = t_0$ with a delayed part $t = t_0 + \tau$. In the Mach-Zehnder interferometer (MZI) there are two optical elements that can be used to vary the path length. The first is a piezo controlled mirror that allows path length changes up to ∼2 μm (with 10 pm resolution). Varying this fine delay allows one to vary the pathlength over one wavelength, i.e., to vary the relative phase, resulting in interference fringes that are monitored on the two APDs by measuring the visibility, defined as $\mathrm{V} = \frac{|I_A - I_B|}{I_A + I_B}$, where I_A, I_B are the intensity counts on each detector. A separate delay stage with a retro reflector (RR) can then change the coarse path length difference between 0–1.2 m ($\tau \sim 0$–4 ns). By scanning the piezo mirror, the visibility $[V(\tau) \equiv |g^{(1)}(\tau)|]$ can be measured as a function of the coarse time delay, which is controlled by the RR This technique is often used to measure the coherence length of a signal (e.g., a laser or single photon). To observe a high visibility, the relative phase of the signal at times $t = t_0$ and τ must be well-defined. Any loss of coherence with time manifests as a reduction in the visibility as a function of τ.

For a charged QD (QD1) we probe in both zero [Fig. 1(d)] and Voigt-field configurations [Fig. 1(e)] when the QD-drive laser detuning is set to zero. The measured coherence time (T_2^*) of the RSF (∼3 ns) in both cases is significantly longer than the transform limit of the radiative transition $2T_1 = 920 \pm 10$ ps [Fig. 1(b)], but similar to the expected spin coherence time, as observed in Ref. [13]. Second, when subjected to a Voigt-magnetic field there is a pronounced oscillation in the $V(\tau)$ ($|g^{(1)}(\tau)|$) where the visibility oscillates from high to almost zero with a frequency of $2\omega_B = 590 \pm 10$ MHz within an exponentially decaying envelope. This oscillation in visibility implies a variation in how well-defined the phase difference is between two time-points of the RSF. Decoherence should cause an exponential decrease in $V(\tau)$ similar to Ref. [13] as was observed for zero field Fig. 1, but a periodic decay and revival of visibility is surprising given the input field is a single frequency. This suggests the laser has been modulated by the spin, particularly as the observed period matches the expected spin precession period.

Our first inference is that the spin modulates the phase of the coherent light state as it precesses. To explore the dynamics we input experimental values from Figs. 1(b) and 1(e) into a master equation model (see Appendix D and Ref. [24]). Figure 1(f) shows a diagram of the energy levels as modeled

by a master equation approach, where two two-level systems are coupled via a magnetic field along the x direction, perpendicular to the optical axis (z), both driven simultaneously by a narrowband driving laser, depicted with linear polarization H. Note that we now express the ground states in the eigenstate of the applied magnetic field (along x) rather than along z as in Fig. 1(a). Through this we can visualize $V(\tau)$ of the RSF, in the spectral domain via a Fourier transform giving a spectrum that is dominated by two sideband peaks at plus/minus the modulation frequency [Fig. 1(g)]. It is clear the RSF neither retains the coherence of the input laser nor inherits the spectrum of the QD. The two peaks in the spectrum are substantially narrower than the spontaneous emission rate (Γ) but broader than the δ-function-like CW drive laser.

To illustrate why this is the case let us consider the spin in eigenstates along the direction of the applied magnetic field (x) ($|\uparrow/\downarrow\rangle_x$) as in Fig. 1(f).The eigenstates are perpendicular to the optical axis and are stationary states that have an energy splitting ($\Delta E = 2\omega_B$) rather than a precession frequency. Suppose the spin is in the state $|\uparrow\rangle_x = |\uparrow\rangle_z + |\downarrow\rangle_z$ and a H-polarized photon is input. Equation (B2) predicts the output state $|\psi(t=\tau)\rangle_{\text{out}} = [|\uparrow\rangle_z - |\downarrow\rangle_z]|V\rangle = |\downarrow\rangle_x|V\rangle$, i.e., a rotated photon state and a flipped spin. This spin flip will result a change in energy of the ground-state spin of $+2\omega_B$ which, to conserve energy, will lead to an energy shifted output photon of $-2\omega_B$. Since the magnetic field is small $2\omega_B < \Gamma$, a H-polarized input photon can equally well couple to the QD spin when it is in the $|\downarrow\rangle_x$ state. Following the same logic this leads to a spin flip in the opposite direction and a photon that is shifted in energy by $+2\omega_B$. The two ground-state spin eigenstates ($|\uparrow/\downarrow\rangle_x$) form a double Λ system that are coupled together via the input field; a scattered photon with energy $-2\omega_B$ will always result in a subsequent scattering at $+2\omega_B$ and visa versa [see illustration Fig. 1(f)]. The bandwidth/coherence time of the RSF is governed by the coherence between these scattering events which is limited by the coherence time of the spin.

This gives rise to the $|g^{(1)}(\tau)|$ that we observe [Fig. 1(e)] resulting from an equal superposition of these two frequency components where the observed oscillation has a one-to-one mapping with the Larmor precession and the decaying envelope represents the T_2^* of the QD spin. One may consider this as either a superposition of frequencies correlated with spin states $|\uparrow\rangle_x$ or $|\downarrow\rangle_x$ or a time evolving phase correlated with the spin states $|\uparrow\rangle_z$ or $|\downarrow\rangle_z$. The system can also be thought of as a set of two mutually coherent Raman scattering processes. Note that neutral QDs do not show the same phenomenon because the lack of ground-state spin means there is no corresponding change in the ground-state energy of the emitter (see Appendix C).

These properties also ensure that the $|g^{(1)}(\tau)|$ (spectrum) is robust to spectral jitter. The inhomogeneous linewidth of the QD in Fig. 1 is $\sim$5 μeV (see Appendix E), substantially larger than the Fourier transform limit (Γ) due to charge noise imposing a time varying stark shift, altering the frequency of the transitions of the QD (ω_{QD}). Our fixed frequency laser (ω_d) will explore a full range of detunings over the measurement and any inhomogeneities in the RSF would manifest as a rapid loss in coherence (<100 ps). We can calculate the effect of spectral jitter on the output RSF spectra using a numerically solved master equation for a driven QD-spin (see Appendix E). In Fig. 1(g) we can see the expected spectra for a range of QD-laser detunings ($\Delta = \omega_{\text{QD}} - \omega_d$). It is clear that the spectrum is largely invariant to this detuning, the central frequency remains fixed at the drive laser frequency (ω_d), and the splitting remains constant. The only variation is in the intensity of the V-polarized RSF, whereas the shape of the $|g^{(1)}(\tau)|$ (spectrum) is robust to imperfections in the light-matter interaction. This provides a simple way to decouple the effects of charge and spin noise in the QD, that avoids time consuming second-order correlations, whilst avoiding real excitation that may provide unwanted feedback between the electron spin and the nuclear spin bath [25,26].

Finally, it is worth considering the photon statistics of the output. Figure 1(c) shows the second-order correlation $g^{(2)}(\tau)$ for the RSF, obtained using a simple Hanbury Brown-Twiss (HBT) interferometer. The resulting correlation shows an antibunching dip where $g^{(2)}(0) < 0.5$ with a timescale determined by spontaneous emission rate (Γ). This antibunching of the RSF on short timescales is identical to that seen for neutral QDs [10] and demonstrates the single particle-like nature of the RSF [11,12]. It is of note that there are no oscillations in the $g^{(2)}(\tau)$ on a ns timescale similar to those in Fig. 1(e). This indicates there is no intensity modulation in the RSF and that the oscillations in the first-order correlations are a pure phase modulation.

The results so far show that the phase of the RSF is modulated by the spin. However, the $g^{(1)}(\tau)$ in Fig. 1(e) is sensitive to phase differences in different parts of the wave function of the RSF, but does not directly measure that the absolute phase is modulated by the spin. To explore this further, we now perform projective measurements of the phase of the RSF compared to the original input laser using a homodyne technique. A simplified schematic of the experiment is shown in Fig. 2(a) (see Appendix F for experimental details). The single-frequency laser is split into two paths, one of which is reflected from the QD micropillar. The RSF and the reference laser, the local oscillator, LO, are then interfered on a beamsplitter and the two-photon coincidences recorded as a function of time delay. This allows for a comparison of the relative phase difference between the RSF and the LO.

When the LO and RSF interfere such that their phases match, signal is directed to one detector (e.g., APD A), whilst when the two arms are out of phase by π, signal is directed to the opposite output (e.g., APD B). Thus we convert the spin dependent global phase seen in Eq. (B2) into which path information. The use of single-photon detectors, APDs, means that projective measurements in the $|\uparrow\rangle_z$, $|\downarrow\rangle_z$ basis at specific time points can be made. A click in APD A(B) projects the spin at $t = 0$ into either $|\uparrow\rangle_z$ or $|\downarrow\rangle_z$, this well-defined spin will subsequently evolve in the magnetic field, and half a precession period later will become orthogonal, leading to an increase in probability of detection in APD B(A). Taking the example where the spin is in $|\uparrow\rangle_z$ at $t = 0$ we use Eq. (B2) to rewrite the output state in terms of spatial mode states $|A\rangle$ and $|B\rangle$ as

$$|\psi\rangle_{\text{out}} = \cos(2\omega_B t)|\uparrow\rangle_z|A\rangle + \sin(2\omega_B t)|\downarrow\rangle_z|B\rangle, \qquad (2)$$

where for simplicity we have considered the case where the intensities, $I_{\text{LO}} = I_{\text{RSF}}$ and $\phi_{\text{LO}} = 0$.These oscillations are

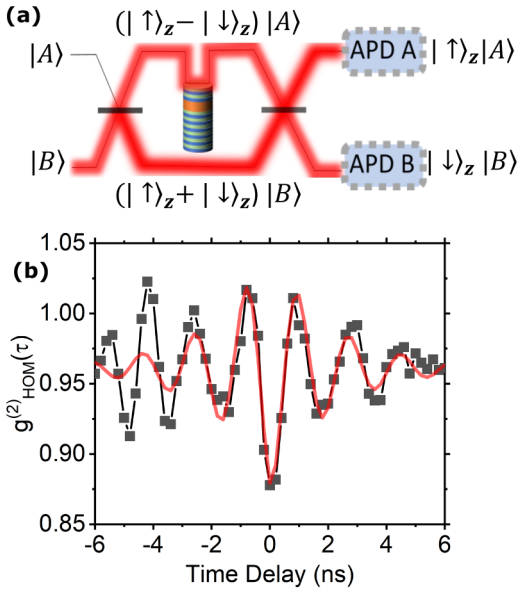

FIG. 2. Panel (a) shows a simplified MZI circuit diagram to illustrate the homodyne measurement performed on QD1. A photon input in $|B\rangle$ will split into an equal superposition $|A\rangle + |B\rangle$. The QD spin in the top arm of the interferometer induces a phase difference on the scattered field depending on the spin orientation, from Eq. (B2) this will give either $|\uparrow\rangle_z|A\rangle$ or $-|\downarrow\rangle_z|A\rangle$. When this is combined with the component of the field in $|B\rangle$ (assuming no phase shift, i.e., $\phi_{LO} = 0$) at the final beamsplitter in the MZI the output becomes $|\uparrow\rangle_z|A\rangle$ or $|\downarrow\rangle_z|B\rangle$. Clearly, if the spin is prepared in a superposition $|\uparrow\rangle_z + |\downarrow\rangle_z$, then the output spatial mode becomes entangled with the spin. (b) $g^{(2)}_{hom}(\tau)$ for the case where the ratio of $I_{RSF} : I_{LO}$ is set to be 1:10. The y intercept is now $\sim$1 as $I_{RSF} << I_{LO}$. The data is fit for positive time delay only. At negative time delay the data displays an increased amplitude which may be related to nuclear spin effects specific to this experiment which are currently under investigation. All data was taken at $B = 108$ mT with a drive field of $P \sim 0.02P_{sat}$ and detected by low efficiency (few %), but fast thin film Si APDs (MPD) with a timing jitter $\sim$64 ps.

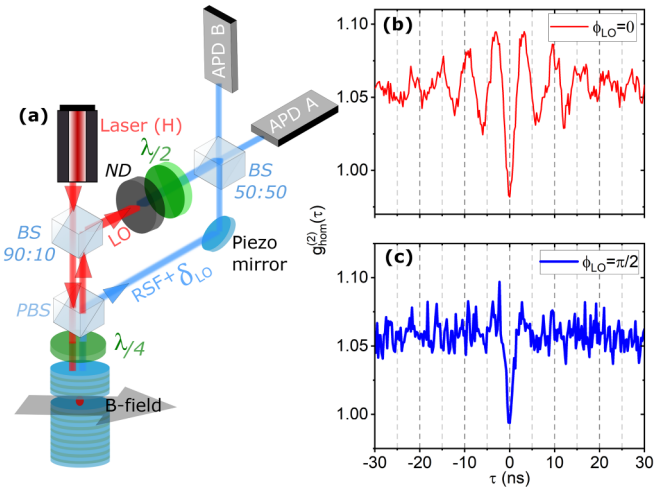

FIG. 3. (a) Schematic of the stabilized homodyne interferometer. A pick off beamsplitter (BS) with a 90% reflectivity selects non-interacting Co-polarized light reflected from the micropillar that is H-polarized, this is then rotated to be V-polarized and constitutes the local oscillator (LO) arm of the interferometer. The path length difference between the LO and RSF arms of the interferometer was made equal using a (2 ps) pulsed laser to within $\sim$100 fs ($\sim$30 μm) where a piezo mirror is responsible for fine control and is used to stabilise the path length difference, which is monitored by interference between the LO and δ_{LO}, where δ_{LO} is a small amount of LO that is allowed into the cross-polarized arm (see Appendix F). The intensity autocorrelations of the homodyne signal $[g^{(2)}_{hom}(\tau)]$ for QD2 in two quadratures are presented for (b) $\phi_{LO} = 0$ and (c) $\phi_{LO} = \pi/2$, using a drive-field power $P \sim 0.1P_{sat}$ and $B = 86$ mT.

evident in the second-order correlation of the homodyne signal $[g^{(2)}_{HOM}(\tau)$, Fig. 2(b)]. One observes the usual antibunching dip at $g^{(2)}_{HOM}(\tau = 0)$ from the RSF, and then a pronounced oscillation with a period of $2\omega_B = 560 \pm 10$ MHz with a coherence time $T_2^* = 2.1 \pm 0.4$ ns in line with the corresponding $|g^{(1)}(\tau)|$ data in Fig. 1(e). This experiment derives the LO directly from the drive laser and it is subject to thermal and mechanical phase drift on a millisecond timescale. However, the setup is stable on the nanosecond timescales between our two-photon counting events (see Appendix F for detailed discussion). The second-order correlations observed here are markedly different from those obtained via a HBT measurement [Fig. 1(c)], demonstrating the interference with the LO maps the phase modulation of the RSF to a spatial mode intensity modulation given by Eq. (B4).

Now let us revisit Fig. 1(e). Equation (1) applied to a precessing spin implies an oscillation in the global phase. The periodic disappearance of the visibility indicates that the phase difference at these points, which correspond to quarter cycles in the precession period, is precisely undefined, i.e., the imparted phase is either 0 or π as the spin evolves into a superposition state when compared to the initial state at $\tau = 0$. To show that in Fig. 1(e) the zero points in visibility correspond to a coherent quantum superposition of scattering off a superposition state, e.g., $|\uparrow_z\rangle \pm |\downarrow_z\rangle$, a different method needs to be applied as the technique in Fig. 2 has limitations that prevent us from learning this. The millisecond instability between the different arms of the MZ interferometer, allows us to interrogate whether the phase of the RSF and LO are the same or different, on a nanosecond timescale for two different projective measurement times τ. However, we lack knowledge of the absolute phase of the time resolved measurement. To map the evolution of the absolute phase of the RSF we need to interfere it with a known, stable, reference phase.

To explore this we modify the simple MZ interferometer set up in Fig. 2(a) to allow for active stabilization of the phase. This allows us to obtain homodyne measurements for arbitrary LO phases. Figure 3(a) shows the modified set up used. Details of the stabilization technique are in the caption and Appendix F. We also use a different QD (QD2) for this experiment. This specific charged QD has a lower in-plane gyromagnetic ratio ($g \sim 0.15$) and a longer $T_2^* \sim$ 13 ns which enables the use of slower more efficient detectors needed for active stabilization (see Appendix F for details).

The resulting two-photon correlations are presented in Fig. 3 which compares the combined homodyne signal from the LO and the RSF for two cases, $\phi_{LO} = 0$ and $\phi_{LO} = \pi/2$ using 256 ps time bins. In Fig. 3(b) we see that for $\phi_{LO} = 0$

we observe a similar homodyne signal to that in Fig. 2(b): an antibunching at $\tau = 0$. then characteristic decaying oscillations in the intensity autocorrelations of the homodyne signal $[g^{(2)}_{\text{hom}}(\tau)]$, with $2\omega_B = 159 \pm 5$ MHz and $T_2^* = 12.5 \pm 1.5$ ns which correspond with the equivalent $|g^{(1)}(\tau)|$ for QD2 (see Appendix G). In contrast for $\phi_{\text{LO}} = \pi/2$ the oscillations disappear [Fig. 3(c)]. What this demonstrates is that at no point can the projective measurement of the phase of the RSF be $\pi/2$: it can only take values of 0 or π(corresponding to $|\uparrow\rangle_z$ or $|\downarrow\rangle_z$).

The fact that one is able to make projective measurements in the $\phi = 0, \pi$ basis but not the $\phi = \pm\pi/2$ basis is not surprising, indeed it is predicted from Eq. (1). and previous theoretical work [27]. The implication of Eq. (1) is that when the spin is in a superposition state in the z basis, e.g., $|\uparrow_z\rangle + |\downarrow_z\rangle$, the phase of the RSF will also be in a superposition state: indeed the state is nonseparable from the spin. The optical selection rules of these QDs, along with our detector bandwidth dictate that only the z component of the spin, along the optical axis, can be projectively measured. Thus when the spin is in the superposition state, the RSF is also in a true quantum superposition state, either $\phi = 0$ or $\phi = \pi$, inseparable from the spin state, $|\uparrow_z\rangle$ or $|\downarrow_z\rangle$. Contrast this with a classical superposition of two fields with phases 0 and π where the result would be a field with phase $\pi/2$. To project the spin in the $|\uparrow/\downarrow\rangle_x$ basis we would need to perform a frequency resolved measurement that could distinguish the two sidebands. However this would necessarily require one to filter with a bandwidth $< \Gamma$ which is known to remove the single-photon-like antibunching feature from the RSF [11,12,28].

We conclude therefore that we have demonstrated a novel quantum modulation of a coherent state laser, resulting in a new quantum state of light that cannot be described classically. While we observe the antibunching behavior of resonance fluorescence seen in neutral QDs with no spin, we find that otherwise the nature of the resonantly scattered field is very different. It does not retain the bandwidth of the coherent excitation but spin properties are directly mapped onto the RSF. These include the dephasing of the spin, but also the fact spin superposition states result in phase superposition of the light. This phase superposition is entirely nonclassical, and nonseparable from the spin.

This is a new class of resonant scattering with important implications for quantum information applications. From a practical point of view, while the interaction is deterministic [18], the bandwidth of the scattered field is several orders of magnitude narrower than that of the emitter. This along with the robustness to spectral jitter expands the scope for interfacing matter and light qubits of very different bandwidths and even wavelengths. A coherently evolving deterministic photon-spin interaction may enable easier distributed entanglement protocols, quantum switches, memories and repeaters, all mediated not by traditional single-photon sources, but a narrow-band photonic "quantum bus" from a single-frequency laser. These principles are likely to apply to a wide range of spin-qubit systems where an optical or microwave interface is used, including diamond color centers, 2D quantum emitters, superconducting qubits, or atomic systems.

ACKNOWLEDGMENTS

The authors acknowledge helpful discussions with A. J. Bennett. This work was funded by the Future Emerging Technologies (FET)-Open FP7-284743 [project Spin Photon Angular Momentum Transfer for Quantum Enabled Technologies (SPANGL4Q)] and the German Ministry of Education and research (BMBF) and Engineering and Physical Sciences Research Council (EPSRC) (EP/M024156/1, EP/N003381/1, and EP/M024458/1). C.S. gratefully acknowledges funding by the German Research Foundation (DPG) within the Project No. PR1749/1.1. P.A. acknowledges financial support provided by EPSRC via Grant No. EP/T001062/1. J.M.L. and S.M. were supported by the Bristol Quantum Engineering Centre for Doctoral Training, EPSRC Grant No. EP/L015730/1.

APPENDIX A: FARADAY ROTATION DUE TO SINGLE QD SPIN

The polarization rotation of the RSF due to the QD spin can be calculated via the reflectivity equation [14,17–19,21]:

$$\begin{aligned} r(\omega_d) &= |r(\omega_d)|e^{i\phi(\omega_d)} \\ &= 1 - \frac{\kappa_k\left(i(\omega_{\text{QD}} - \omega_d) + \frac{\gamma}{2}\right)}{\left(i(\omega_{\text{QD}} - \omega_d) + \frac{\gamma}{2}\right)\left(i(\omega_c - \omega_d) + \frac{\kappa_k}{2}\right) + g^2}, \end{aligned} \tag{A1}$$

where $r(\omega_d)$ is the frequency dependant reflectivity, ω_{QD} is the QD frequency, ω_c is the cavity frequency and ω_d the frequency of the probing laser. The cavity QED parameters g and κ_k represent coupling constants between the QD and the cavity mode and the cavity mode and the input/output electromagnetic field modes, respectively. γ represents a loss and is the rate the QD couples to noncavity modes. Note that this complex function can be expressed as $r(\omega_d) = |r(\omega_d)|e^{i\phi(\omega_d)}$, where $\phi(\omega_d)$ is the phase of the reflected light. We have made the simplification that the cavity is single sided appropriate for our micropillar design.

This can be rewritten in terms of cavity parameters including the β factor which is a parameter that denotes the fraction of spontaneous emission (given by Γ) that couples into the cavity mode vs all available modes, i.e., $\beta = \frac{\Gamma}{\Gamma+\gamma}$. It is 1 for a perfect cavity, i.e., all spontaneous emission couples to the cavity mode and there are no losses:

$$r(\omega_d) = 1 - \frac{i(\omega_{\text{QD}} - \omega_d) + \frac{(1-\beta(\omega_d))(\Gamma(\omega_d)+\gamma)}{2}}{i(\omega_{\text{QD}} - \omega_d) + \frac{(1-\beta(\omega_d))(\Gamma(\omega_d)+\gamma)}{2} + \frac{\beta(\omega_d)(\Gamma(\omega_d)+\gamma)}{4}}.$$

Now suppose we have the QD in a superposition state:

$$|\psi\rangle_{\text{spin}} = |\uparrow\rangle_z + |\downarrow\rangle_z. \tag{A2}$$

The QD selection rules dictate that the $|\uparrow\rangle_z$ will only couple to photons in $|L\rangle$, and $|\downarrow\rangle_z$ will only couple to photons in $|R\rangle$. If we scatter an H-polarized photon, then after interaction the output state will be

$$\begin{aligned}|\psi\rangle_{\text{in}} &= |\psi\rangle_{\text{spin}} \otimes (|R\rangle + |L\rangle) \rightarrow \\ |\psi\rangle_{\text{scat}} &= (|r_c||R\rangle + |r_h|e^{i(\phi_h-\phi_c)}|L\rangle)|\uparrow\rangle_z \\ &\quad + (|r_h|e^{i(\phi_h-\phi_c)}|R\rangle + |r_c||L\rangle)|\downarrow\rangle_z.\end{aligned}$$

Here, $|r_h|$ and ϕ_h represent the amplitude and phase modulation via interaction with a cavity coupled to an active optical transition of the QD. $|r_c|$ and ϕ_c represent the input field scattering from an empty cavity. In our experiment we then pass this through a linear polarizer and collect only the cross-polarized signal that is V polarized ($|V\rangle\langle V|$) this leaves is with a cross polarized state:

$$|\psi\rangle_{\text{cross}} = [|\uparrow\rangle_z - |\downarrow\rangle_z]|V\rangle, \tag{A3}$$

which will occur with a probability amplitude given by $\frac{i}{2\sqrt{2}}(|r_c| - |r_h|e^{i(\phi_h-\phi_c)})$.

It is clear in this scenario our input H-polarized photon will be flipped to V-polarized and our spin will flip from $|\uparrow\rangle_z + |\downarrow\rangle_z \rightarrow |\uparrow\rangle_z - |\downarrow\rangle_z$. The spin flip occurs when a superposition state is present and the phase of the photon is undefined, i.e., the phase of the photon has not been projected similar to Ref. [27]. The term $\frac{i}{2\sqrt{2}}(|r_c| - |r_h|e^{i(\phi_h-\phi_c)})$ is a complex number representing the probability amplitude; it is a constant that depends on system parameters, and in the main paper we have removed this coefficient by setting it equal to 1 which corresponds to an ideal lossless light matter interaction. These parameters can be found using Eq. (A2) where under resonant conditions when $\beta = 1$, we find $|r_c| = |r_h| = 1$ and $\phi_h - \phi_c = \pi$. The micropillar we use does not have perfect light matter interaction (i.e., $0.5 < \beta -$ factor<1), this results in $|r_c|$, $|r_h|$ being <1. This is simply a reduction in the amplitude, i.e., the number of scattering events that result in a cross polarized photon, but every time a photon is scattered into V there is a corresponding spin flip.

Examining Eq. (A3) allows us to understand some of the basics of the interaction and output RSF. If we perform a measurement that is not phase sensitive, then the result of the above spin photon interaction is photon whose polarization has rotated from H to V accompanied by a spin flip of the spin state of the QD. However, if we implement a phase sensitive measurement, then it becomes possible to distinguish the $|\uparrow\rangle_z$, and $-|\downarrow\rangle_z$ states in Eq. (A3). due to the π phase difference in their global phase. This z-basis measurement can be done with the interferometric setups described in the main paper and in the section later in the the Appendix (Fig. 7).

APPENDIX B: SPIN INSIDE A MACH-ZEHNDER INTERFEROMETER

The phase modulation we presented in the previous section is difficult to parse in a discussion of spin-photon entanglement. It becomes much more obvious when we map this into spatial modes. This can be done via including the spin in one am of a balanced MZI (Fig. 4). This is precisely how we achieve the homodyne correlations we present in the main paper. The interaction described below has a one-to-one mapping with previous work described for photonic crystal waveguides [30]. If we consider the spin in some arbitrary superposition state, then $\alpha|\uparrow\rangle + \beta|\downarrow\rangle$ and we include it in a system with two possible spatial modes $|A\rangle$ and $|B\rangle$. If we input a photon $|A\rangle$, then when it reaches the first beamsplitter of the MZI it will we will be left with the photon just after the beamsplitter being in the state $\frac{1}{\sqrt{2}}(|A\rangle + |B\rangle)$. The result is a initial state for the spin photon system just after first beamsplitter but before scattering from spin of

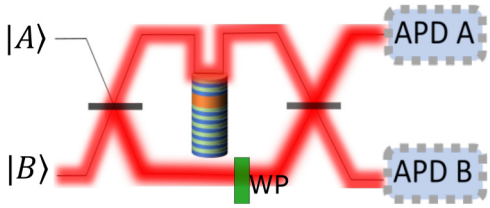

FIG. 4. MZI containing a spin in the top arm only this maps directly to the homodyne correlations in the main paper and in Appendix B below. WP represents a half waveplate used to ensure an overlap of the output polarization at the final beamsplitter.

$$\frac{1}{\sqrt{2}}(|A\rangle + |B\rangle) \otimes \alpha|\uparrow\rangle_z + \beta|\downarrow\rangle_z. \tag{B1}$$

We will now make the simplifying assumption that our interaction is perfect and will use the spin photon interaction outlined in the main paper, namely:

$$\begin{aligned}|\psi\rangle_{\text{in}} = |\uparrow\rangle_z|H\rangle \rightarrow |\psi\rangle_{\text{out}} = |\uparrow\rangle_z|V\rangle, \\ |\psi\rangle_{\text{in}} = |\downarrow\rangle_z|H\rangle \rightarrow |\psi\rangle_{\text{out}} = -|\downarrow\rangle_z|V\rangle.\end{aligned} \tag{B2}$$

Since the polarization of the photons is not useful when distinguishing the two possible spin states and we can drop it from our discussion from this point onward. This can be achieved experimentally via a half waveplate in the bottom arm of the MZI to ensure that the the polarization in both arms is the same when the two parts of the photon overlap on the final beamsplitter.

After interacting with the spin but before we reach the final beamsplitter we can write out in intermediate state

$$\begin{aligned}|\psi\rangle_{\text{in}} &\rightarrow |\psi\rangle_{\text{int}} \\ &= \frac{1}{\sqrt{2}}(|A\rangle[\alpha|\uparrow\rangle_z - \beta|\downarrow\rangle_z] + |B\rangle[\alpha|\uparrow\rangle_z + \beta|\downarrow\rangle_z]).\end{aligned}$$

Only the component of the photon that traveled through the top arm of the MZI will interact with the spin leading to the minus sign which is highlighted in red. The action of the second beamsplitter in the MZI will leave us with two possible output states with orthogonal spatial modes:

$$\begin{aligned}|A\rangle_{\text{out}} = \alpha|\uparrow\rangle_z, \\ |B\rangle_{\text{out}} = \beta|\downarrow\rangle_z.\end{aligned} \tag{B3}$$

It is obvious now how one can achieve spin photon entanglement as the two possible spin states scatter the output photon into two orthogonal spatial modes. We have used an arbitrary spin state with complex probability amplitudes α and

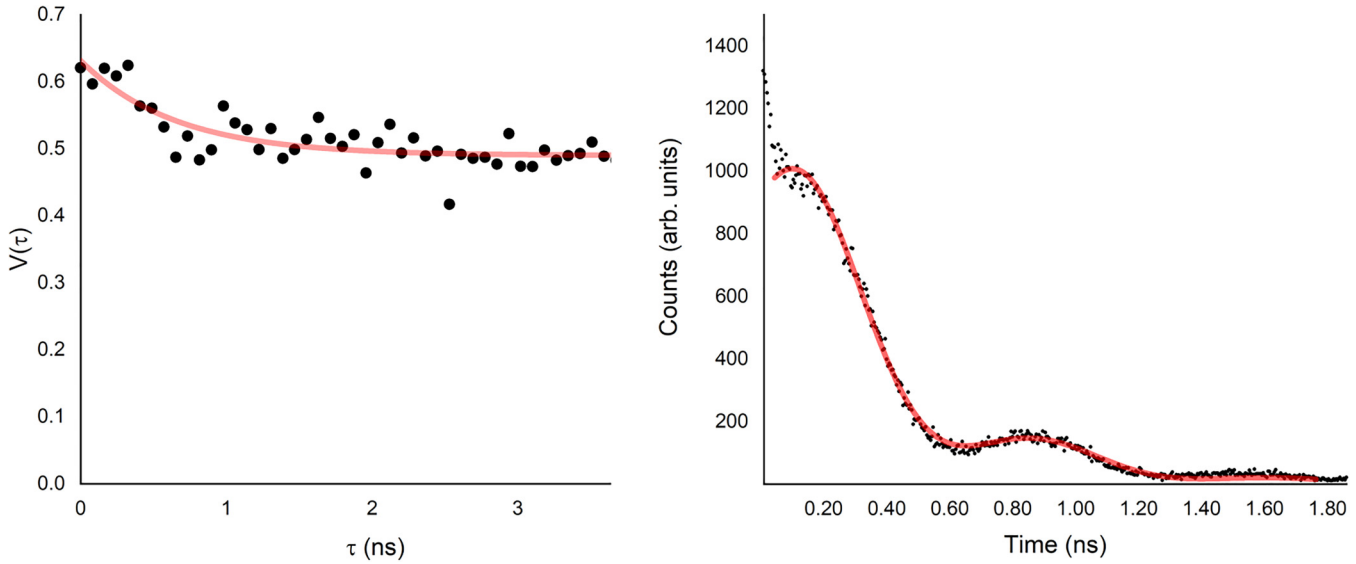

FIG. 5. The figure on the left is the visibility of the interference measured using the setup in Fig. 1(a) from the main paper for a neutral QD. On the right-hand side is lifetime for the neutral QD measured under pulsed excitation. Both data sets are recorded at a $B \sim 100$ mT Voigt field.

β. We can include a time dependence in these probability amplitudes if we make a simplifying assumption that the duration of the input photon is much shorter than any time dynamics of the of the spin. Alternately it can be valid when we are able to project the photon on timescales much faster that the spin dynamics. Doing this we are able to write the output state for the MZI in the presence of a precessing spin as we have in Eq. (2) in the main paper as

$$|\psi\rangle_{\text{out}} = \cos(2\omega_B t)|\uparrow\rangle_z|A\rangle + \sin(2\omega_B t)|\downarrow\rangle_z|B\rangle. \tag{B4}$$

APPENDIX C: NEUTRAL QD

We also perform a reference measurement on a neutral QD so the $|g^{(1)}|$ can be compared to the results in the main paper. This can be seen in Fig. 5. Here we see a small initial decay in the coherence as a result of real excitation which then levels out to give a flat $V(\tau)$ corresponding to the RSF field inheriting the coherence of the laser [31]. We also measure the lifetime as we did for the charged QD. Interestingly the decay from real excitation now contains oscillations. These are a beating between the two possible excited state transitions. This is possible as they share a common ground state unlike the charged QD of the main paper. The oscillations correspond to a line splitting ~0.9 μeV, likely due to fine structure splitting that the $B \sim 100$ mT Voigt field applied here is unlikely to have overcome. The observed decay time corresponds to a Fourier transform limited linewidth ~1.6 μeV, hence this QD exhibits a subnatural linewidth splitting. The amplitude modulation that is observed for the neutral QD here is in contrast with the charged QD that contains a ground-state spin, where there is no beating in the optical lifetime (0.3 μeV Zeeman splitting). This is due to the fact that output photons become entangled with the ground-state spin preventing interference. This leaves a modulation that is purely on the phase of the RSF field.

APPENDIX D: MASTER EQUATION MODEL OF OPTICALLY ACTIVE CHARGED QD SPIN

The system under consideration in this work can be modeled as a four-level system (FLS), with two ground states and two excited states. The ground states form an effective spin 1/2 system whose basis states are given as $|\uparrow\rangle$ and $|\downarrow\rangle$, quantized along the growth axis of the QD. The $|\uparrow\rangle(|\downarrow\rangle)$ state is optically coupled to the trion state $|\uparrow\rangle(|\downarrow\rangle)$ by right(left) circularly polarized light. The FLS is coupled to a cavity which has two polarized modes, a_L and a_R, representing left and right circular polarization, respectively. These cavity modes are then coupled to the external electromagnetic field with modes $r_{k,L}$ and $r_{k,R}$ where again L and R denote left and right circular polarization. With this we can express the Hamiltonian of the full system as $H = H_0 + H_B + H_I$, where H_0 represents the energy of the FLS and cavity, H_B represents the energy of the bath modes and H_I describes the interactions between the subsystems. Furthermore, these can be expressed in terms of the system parameters as follows (note we set $\hbar = 1$):

$$\begin{aligned} H_0 &= \omega_{\text{QD}} P_e + \omega_B \sigma_x + \omega_c (a_R^\dagger a_R + a_L^\dagger a_L) \\ H_B &= \sum_k \omega_k (r_{k,R}^\dagger r_{k,R} + r_{k,L}^\dagger r_{k,L}) \\ H_I &= g(S_-^R a_R^\dagger + S_-^L a_L^\dagger + \text{H.c.}) \\ &\quad + \sum_k \kappa_k (r_{k,R} a_R^\dagger + r_{k,L} a_L^\dagger) + \text{H.c.}, \end{aligned}$$

where ω_{QD} is the energy of the excited trion states, $P_e = |\Uparrow\rangle\langle\Uparrow| + |\Downarrow\rangle\langle\Downarrow|$ is the projection operator on to the excited state subspace, $\omega_B \sigma_x = \omega_B(|\uparrow\rangle\langle\downarrow| + |\downarrow\rangle\langle\uparrow|)$ represents the coupling of the ground states caused by the external magnetic field in the Voigt geometry, ω_c is the energy of the cavity modes, ω_k is the energy of the kth field mode, $S_-^R = |\uparrow\rangle\langle\Uparrow|$; $S_-^L = |\downarrow\rangle\langle\Downarrow|$ are dipole operators and finally g and κ_k

represent coupling constants between the system and the cavity and the cavity and the electromagnetic field, respectively. To calculate the quantities we are interested in requires a master equation for the dynamics of the FLS. To arrive at this we follow methods described in Ref. [32]. Hence, the port modes are traced out giving a master equation for the cavity and the FLS in the Born-Markov approximation. Furthermore, the cavity modes can be eliminated adiabatically [33] leading to the following master equation written in a frame rotating at the drive-field frequency

$$\dot{\rho}(t) = -i[H, \rho(t)] + \sum_{k=R,L} L_k \rho(t) L_k^\dagger - \frac{1}{2}\{L_k^\dagger L_k, \rho(t)\} + \mathcal{D}(\rho), \quad \text{(D1)}$$

with

$$H = \Delta P_e + \omega_B \sigma_X + (\Omega_R S_-^R + \Omega_L S_-^L + \text{H.c.}). \quad \text{(D2)}$$

The Lindblad operators responsible for optically induced dissipation have the form $L_{R/L} = \sqrt{\Gamma} S_-^{R/L}$ and $\mathcal{D}(\rho) = \frac{\gamma_{pd}}{2}$ $[\sigma_x \rho(t) \sigma_x - \frac{1}{2}\{\sigma_x^2, \rho(t)\}]$ describes the additional process of pure-dephasing with a rate γ_{pd}. Here Δ is the renormalized detuning, Γ is the Purcell enhanced decay rate and $\Omega_{R/L}$ represents the driving parameters of the system. This adiabatic approximation is valid in the regime where the cavity bandwidth is much greater then the bandwidth of the system dynamics.

The main quantity of interest is the the visibility, $V(\tau)$, of the RSF as measured by a MZI. We define this as the magnitude of the steady-state first-order correlation function:

$$V(\tau) = \left| g^{(1)}(\tau) \right|. \quad \text{(D3)}$$

To calculate this steady-state correlation function we express it in terms of the vertically polarized output electric field:

$$g^{(1)}(\tau) = \langle \mathbf{E}_V^{(-)}(\tau) \mathbf{E}_V^{(+)}(0) \rangle \propto \langle S_+^V(\tau) S_-^V(0) \rangle. \quad \text{(D4)}$$

Here $S_-^V(t) = \frac{1}{\sqrt{2}}(S_-^R(t) - S_-^L(t))$ is the vertically polarized dipole operator. The final proportionality in Eq. (7) can be derived by applying input-output theory [34] to the system and holds when the input field is horizontally polarized. Another interesting quantity is the cross-polarized emission spectrum. This can be calculated from the first-order correlation function via a Fourier transform:

$$S(\omega - \omega_D) = \int_{-\infty}^{\infty} g^{(1)}(\tau) e^{-i\omega\tau} d\tau. \quad \text{(D5)}$$

With the desired quantities now expressed in terms of operators of the FLS they can be calculated by solving the master equation numerically. Here this was done via QuTiP [35], which we use to generate the plots in Fig. 1 in the main paper. This spectrum contains some rich and interesting physics. It demonstrates different frequency distributions depending on the relative strength of driving and precession processes. These effects can be described analytically by solving the above master equation in the weak driving regime. The details of this is beyond the scope of this work and a thorough analysis of this system can be found in Ref. [24].

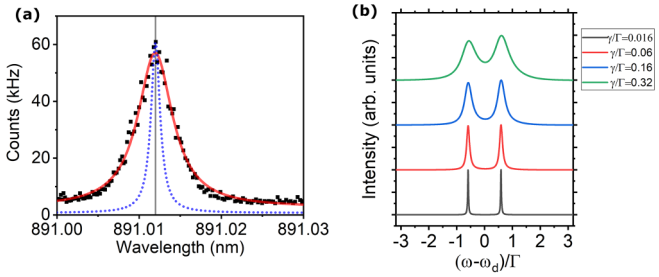

FIG. 6. (a) The RSF spectrum as a function of the drive-field laser wavelength. Data is recorded by stepping the wavelength single-frequency laser and integrating the number of counts in the V-polarized channel over a 1 second interval at each wavelength. The blue dashed line is an indicator that represents the transform limited result derived from the observed spontaneous emission lifetime. The gray solid line represents the drive-field laser spectrum for the case when $\Delta = 0$. (b) The effect that varying the pure dephasing rate in the master equation has on the RSF spectrum for the case when the QD-laser detuning is set to $\Delta/\Gamma = 0.5$. It is clear that as the pure dephasing rate is decreased the asymmetry in the RSF disappears.

APPENDIX E: SPECTRAL JITTER AND DEPHASING

In Fig. 1 in the main paper we use the master equation model from the previous section to predict how the RSF spectrum varies with QD-laser detuning. Figure 6(a) above shows the inhomogeneously broadened spectra of QD1 described in Figs. 1 and 2 in the main paper. The data is accumulated by tuning the single-frequency drive laser through the QD transition where we observe a RSF signal with a Lorentzian line-shape and bandwidth of ∼5 μeV. This is substantially broader than the ∼1.3 μeV of the transform limited line and shows the extent to which spectral jitter broadens the observed transitions. Over the course of an experimental run (> seconds) if our single-frequency laser remains at a fixed frequency then the QD will be subjected to this slow (∼μs) spectral jitter and the Fourier limited line will (randomly) explore a full range of detunings. We showed in Fig. 1(g) of the main paper that the output RSF is invariant to this detuning and thus remains unchanged in all aspects besides its intensity.

At moderate values for the QD-laser detuning ($\Delta/\Gamma = \pm 0.5$) there is an observable discrepancy between the peak heights in the RSF spectrum. This is an artefact of the the way dephasing is modeled in the master equation. To ensure the master equation can describe the experiment we need to incorporate a term that describes spin dephasing. The established way to do this is by adding a Lindblad term $\mathcal{D}(\rho)$. This models a pure dephasing process (γ) which is the equivalent to the T_2 coherence time for the spin. Whilst the RSF from the QD-spin is invariant to spectral wander that stark shifts the transitions it is not insensitive to changes in the Larmor frequency (Zeeman splitting). These processes fall more broadly under the umbrella of spin noise. Here slow (of order μs) variations to the nuclear spin bath cause a time varying Overhauser field across the QD. This dynamically changes the effective B-field applied to the QD-spin and changes the line splitting in the RSF. When this is averaged over longer timescales (>seconds) it leads

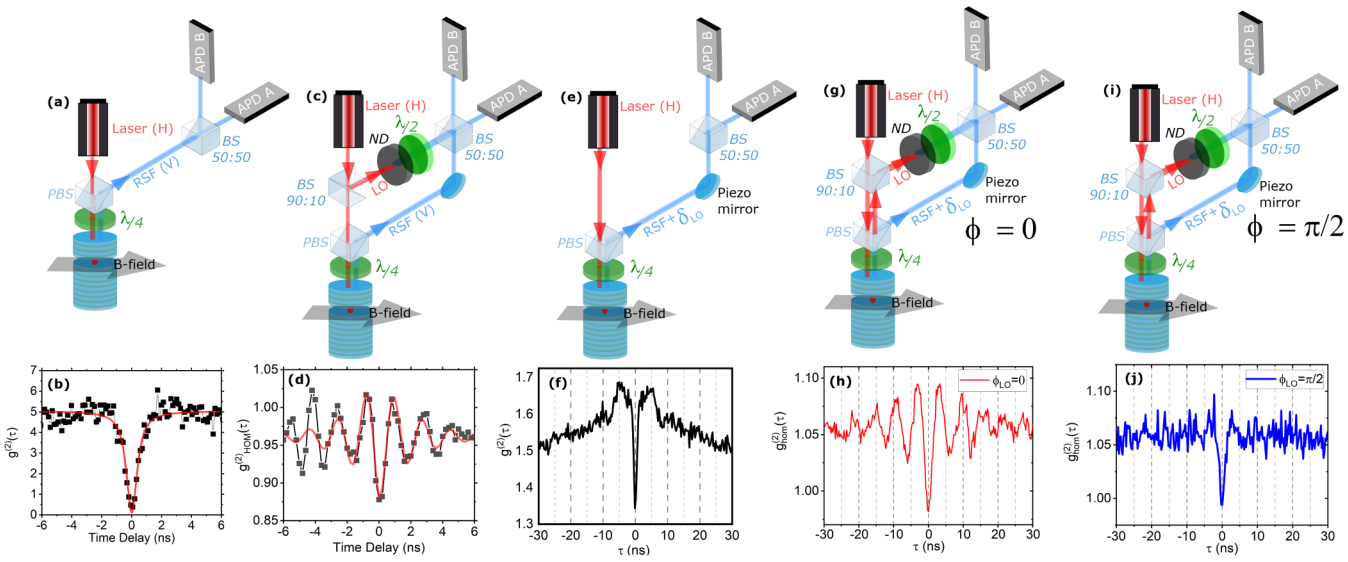

FIG. 7. (a) Hanbury Brown-Twiss setup used to measure antibunching $g^{(2)}(t)$ measurement of the RSF. (b) The measured $g^{(2)}(t)$ data for QD1. (c) Shows the homodyne setup that is used to measure the non phase locked second-order correlation of the homodyne signal $g^{(2)}_{\rm hom}(t)$, with the data for QD1 presented in panel (d). This measurement does not implement any phase locking of the LO which is derived by splitting off a small amount of the input laser and overlapping it with the RSF on the final beam-splitter. For active stabilization it is necessary to allow a small amount of LO ($\delta_{\rm LO}$) into the RSF arm of the MZI. This leads to a signal in the RSF arm that is roughly a 50:50 mixture of RSF and LO. To measure the second-order correlation of this signal we use the setup in panel (e). (f) Shows the $g^{(2)}(t)$ for the field RSF + $\delta_{\rm LO}$ where the intensities $I_{\delta_{\rm LO}} \sim I_{\rm RSF}$ for QD2. The main feature in the correlation is a small antibunching dip whose depth is limited by the presence of $\delta_{\rm LO}$ along with the detector timing resolution of ∼300 ps. There are no clear oscillations on a ns timescale outside of the central antibunching feature confirming that there is no measurable homodyne signal at the PBS using this technique. (g) Shows the homodyne setup used to measure $g^{(2)}_{\rm hom}(t)$ when $\phi_{\rm LO} = 0$. The LO is derived from the Co-polarized (H) channel using pick off light from a 90:10 (R:T) beam-splitter. The path length between the LO and RSF arms of the MZI is maintained via monitoring the interference between LO and $\delta_{\rm LO}$, and active feedback provided via a movable piezo mirror, the data for QD2 is shown in panel (h). To change the measurement basis we can stabilise the path length difference between the RSF and LO arm at different points such as in panel (i) where $\phi_{\rm LO} = \pi/2$ with the $g^{(2)}_{\rm hom}(t)$ for QD2 presented in panel (j). Data from QD1 in panels (b) and (d) are taken with an applied external magnetic field (Voigt) of $B = 108$mT, and correlations recorded with thin film APDs with timing jitter of 64 ps. Data from QD2 in panels (f), (h), and (j) are taken at $B = 86$mT with standard Si APDs with timing jitter of 300 ps.

to an inhomogeneous broadening where experimentally one measures the T_2^*, an ensemble average coherence time. Since our measurements cannot distinguish the T_2 from the T_2^* we use a model with pure dephasing, i.e., T_2. This represents a worse case scenario for the dephasing of the spin as the underlying T_2 in our system is likely significantly longer and we are dominated by inhomogeneous processes.

The pure dephasing model is responsible for the discrepancies in peak heights in the RSF when using the master equation model. We can see from Fig. 6(b) as the rate of pure dephasing approaches the that of the spontaneous emission lifetime the asymmetry in the RSF spectrum is more pronounced. This is due to the addition of a competing incoherent process that becomes sensitive to the small Zeeman splitting at moderate detunings. Clearly, in the limit where the pure dephasing is small this effect is not observed and the underlying RSF spectrum is derived from coherent processes and the spectrum retains its symmetry. By using a model of pure dephasing we over emphasise this effect where in the limit of no pure dephasing and the observed coherence is entirely limited by inhomogeneous effects then the spectrum would be symmetric for all values of Δ. A more detailed study of the dephasing mechanisms can be found in Ref. [24].

APPENDIX F: SECOND-ORDER CORRELATIONS AND HOMODYNE MEASUREMENTS

In the main paper we perform several second-order correlation measurements of the RSF and here we include more detailed setup diagrams in Fig. 7. Figure 7(a) shows how we measure a simple HBT correlation to probe the single-photon nature of the RSF. Figure 7(b) shows how we measure the second order correlation of the homodyne signal from QD1. For this we use low efficiency thin film Si APDs with a timing jitter of 64 ps. This provides us with sufficient timing resolution to resolve the oscillations in the homodyne signal due to the evolving spin state (approximately 2 ns period). This experiment derives the LO directly from the drive laser and it is not phase stable. There is a slow (ms) drift in $\phi_{\rm LO}$ which over the long timescale (hours) it takes to gather statistics for the $g^{(2)}_{\rm hom}$ which means we sample all possible values of $\phi_{\rm LO}$. However, this does not impact the two photon correlations used to measure the fast (ns) spin dynamics over which timescales $\phi_{\rm LO}$ remains fixed. The end result is a sum of homodyne correlations for all possible values of $\phi_{\rm LO}$ against which the observed oscillations are robust. Another side effect of the slow phase drift is that a click in one of the measurement APDs does not provide an absolute measurement of the

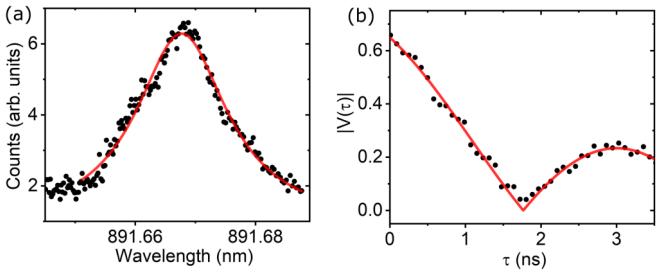

FIG. 8. (a) The RSF response as a single-frequency laser is tuned through the QD2 transition for a drive strength $\omega \sim 0.1\Gamma$ in a $B \sim 86$ mT Voigt field. The measured linewidth is ∼28 μeV this is considerably broader than QD1 due to an increase in the spectral jitter for this particular QD (b) Measurement of $|g^{(1)}(\tau)|$ for QD2 under the same driving conditions. Fitting the data yields a time period for the precession ∼6.2 ns or a Larmor precession frequency $2\omega_B \sim 157$ MHz, i.e., a Zeeman splitting ∼0.1 μeV. This matches the timescales recorded for the homodyne measurement in the main paper.

spin state. Whilst it still represents a projective measurement we lack knowledge of the precise phase difference between the two arms of the interferometer at the time the photon is detected.

For phase stable homodyne correlations we use QD2. This specific charged QD has a lower in-plane gyromagnetic ratio ($g \sim 0.15$) and a longer $T_2^* \sim 13$ ns. As such we can measure correlations using standard Si-APDs (30% efficient) with a timing jitter ∼300 ps improving detected counts by an order of magnitude. This allows us to obtain sufficient count rate to implement a phase locked interferometer on a ms timescale. We derive the local oscillator from the copolarized (H) channel from the setup in Fig. 7(a) which is composed of light that has not interacted with the QD, i.e., mismatched to the cavity mode and has reflected directly from the top of the micropillar. The fact that both the LO and the RSF signal have the same optical path to and from the QD micropillar sample drastically reduces the phase noise allowing active feedback to become a viable means to stabilise the interferometer. The LO is attenuated by a neutral density filter (ND) such that $I_{\mathrm{LO}} \sim 10 I_{\mathrm{RSF}}$ and rotated to be V-polarized. To implement the phase lock a small amount of LO (δ_{LO}) is introduced into the RSF arm using a quarter waveplate (∼1^o rotation) [see Fig. 7(e)] such that the ratio of intensities of $I_{\delta_{\mathrm{LO}}} : I_{\mathrm{RSF}}$ is approximately 1:1 in the cross-polarized (V) output. The δ_{LO} component then provides an interference signal when combined with the LO at the final BS that is monitored on a 15 ms timescale and is used to feedback to a piezo actuated mirror to fix the phase difference between the two arms of the interferometer. By choosing different points of the interference fringe we can change the relative phase between the RSF arm and the LO arm and thus change the quadrature that we measure. This allows the whole setup to be phase stabilized all the way to the sample. The noise is around 15% about a chosen set-point as such the LO phase has the same corresponding uncertainty. The mixture of δ_{LO} and RSF will result in a very weak self homodyne signal at the PBS, but it is not significant enough to affect the overall resulting interference at the final BS. This is evident in the second-order correlation of this signal for QD2 [Fig. 7(f)] where data is collected by blocking the LO arm of the interferometer so the only signal at the final BS is RSF + δ_{LO} [Fig. 7(e)]. The main feature in the correlation is a small antibunching dip whose depth is limited by the presence of δ_{LO} along with the detector timing resolution of ∼300 ps. There are no pronounced oscillations, unlike Figs. 7(d) and 7(h) when the LO arm in unblocked.

APPENDIX G: SUPPLEMENTARY DATA FOR QD2

For stabilized homodyne measurements we use QD2 this is due to its lower in plane gyromagnetic ratio. Figure 8(b) shows the $|g^{(1)}(\tau)|$ which corresponds to a Larmor precession frequency of $2\omega_B \sim 157$ MHz (∼6 ns period) for $B \sim 86$ mT. This is approximately three times slower than QD1 which means the two photon correlations from the homodyne interferometer can be captured with standard Si-APDs with around 30% efficient detection with a timing uncertainty ∼300 ps. Statistics for the each homodyne measurement are gathered over approximately 24 h. Note we do not use the same thin film APDs that are deployed to measure QD1 as the efficiency is only a few % which for this particular measurement makes two photon correlations, and stabilizing the interferometer challenging.

The disadvantage of QD2 is that the slow precession frequency means the $|g^{(1)}(\tau)|$ is less reliable. In order for the fitted data to be reliable we need to observe at least one full oscillation, while the data in Fig. 8(b) only contains a half period. This is why in the main paper we focus on QD1 for a discussion of the dynamics observed in the $|g^{(1)}(\tau)|$, and also why the values quoted above are only given approximately.

[1] R. Hanbury Brown and R. Q. Twiss, A test of a new type of stellar interferometer on sirius, Nature (London) **178**, 1046 (1956).
[2] H. J. Kimble, M. Dagenais, and L. Mandel, Photon antibunching in resonance fluorescence, Phys. Rev. Lett. **39**, 691 (1977).
[3] R. J. Glauber, The quantum theory of optical coherence, Phys. Rev. **130**, 2529 (1963).
[4] B. R. Mollow, Power spectrum of light scattered by two-level systems, Phys. Rev. **188**, 1969 (1969).
[5] W. Heitler, *The Quantum Theory of Radiation* (Dover Publications, Mineola, NY, 2010).
[6] D. P. Vincenzo, The physical implementation of quantum computation, Fortschr. Phys. **48**, 771 (2000).
[7] E. Knill, R. Laflamme, and G. J. Milburn, A scheme for efficient quantum computation with linear optics, Nature (London) **409**, 46 (2001).
[8] L.-M. Duan and H. J. Kimble, Scalable photonic quantum computation through cavity-assisted interactions, Phys. Rev. Lett. **92**, 127902 (2004).

[9] E. Waks and J. Vuckovic, Dipole induced transparency in drop-filter cavity-waveguide systems, Phys. Rev. Lett. **96**, 153601 (2006).

[10] C. Matthiesen, A. N. Vamivakas, and M. Atatüre, Subnatural linewidth single photons from a quantum dot, Phys. Rev. Lett. **108**, 093602 (2012).

[11] L. Hanschke, L. Schweickert, J. C. López Carreño, E. Schöll, K. D. Zeuner, T. Lettner, E. Z. Casalengua, M. Reindl, S. F. Covre da Silva, R. Trotta, J. J. Finley, A. Rastelli, E. del Valle, F. P. Laussy, V. Zwiller, K. Müller, and K. D. Jöns, Origin of antibunching in resonance fluorescence, Phys. Rev. Lett. **125**, 170402 (2020).

[12] J. C. L. Carreño, E. Z. Casalengua, F. P. Laussy, and E. del Valle, Joint subnatural-linewidth and single-photon emission from resonance fluorescence, Quant. Sci. Technol. **3**, 045001 (2018).

[13] Z. Sun, A. Delteil, S. Faelt, and A. Imamoğlu, Measurement of spin coherence using Raman scattering, Phys. Rev. B **93**, 241302(R) (2016).

[14] C. Y. Hu, A. Young, J. L. O'Brien, W. J. Munro, and J. G. Rarity, Giant optical Faraday rotation induced by a single-electron spin in a quantum dot: Applications to entangling remote spins via a single photon, Phys. Rev. B **78**, 085307 (2008).

[15] C. Bonato, F. Haupt, S. S. R. Oemrawsingh, J. Gudat, D. Ding, M. P. van Exter, and D. Bouwmeester, CNOT and bell-state analysis in the weak-coupling cavity QED regime, Phys. Rev. Lett. **104**, 160503 (2010).

[16] N. H. Lindner and T. Rudolph, Proposal for pulsed on-demand sources of photonic cluster state strings, Phys. Rev. Lett. **103**, 113602 (2009).

[17] P. Androvitsaneas, A. B. Young, C. Schneider, S. Maier, M. Kamp, S. Höfling, S. Knauer, E. Harbord, C. Y. Hu, J. G. Rarity, and R. Oulton, Charged quantum dot micropillar system for deterministic light-matter interactions, Phys. Rev. B **93**, 241409(R) (2016).

[18] P. Androvitsaneas, A. B. Young, J. M. Lennon, C. Schneider, S. Maier, J. J. Hinchliff, G. S. Atkinson, E. Harbord, M. Kamp, S. Höfling, J. G. Rarity, and R. Oulton, Efficient quantum photonic phase shift in a low q-factor regime, ACS Photon. **6**, 429 (2019).

[19] A. Auffeves-Garnier, C. Simon, J.-M. Gerard, and J.-P. Poizat, Giant optical nonlinearity induced by a single two-level system interacting with a cavity in the purcell regime, Phys. Rev. A **75**, 053823 (2007).

[20] M. Atature, J. Dreiser, A. Badolato, and A. Imamoglu, Observation of Faraday rotation from a single confined spin, Nat. Phys. **3**, 101 (2007).

[21] A. B. Young, R. Oulton, C. Y. Hu, A. C. T. Thijssen, C. Schneider, S. Reitzenstein, M. Kamp, S. Höfling, L. Worschech, A. Forchel, and J. G. Rarity, Quantum-dot-induced phase shift in a pillar microcavity, Phys. Rev. A **84**, 011803(R) (2011).

[22] S. Sun, H. Kim, G. S. Solomon, and E. Waks, A quantum phase switch between a single solid-state spin and a photon, Nat. Nanotechnol. **11**, 539 (2016).

[23] C. Arnold, J. Demory, V. Loo, A. Lemaître, I. Sagnes, M. Glazov, O. Krebs, P. Voisin, P. Senellart, and L. Lanco, Macroscopic rotation of photon polarization induced by a single spin, Nat. Commun. **6**, 6236 (2015).

[24] T. Nutz, S. T. Mister, P. Androvitsaneas, A. Young, E. Harbord, J. G. Rarity, R. Oulton, and D. P. S. McCutcheon, Coherent scattering from coupled two-level systems, arXiv:2306.08439.

[25] A. V. Kuhlmann, J. Houel, A. Ludwig, L. Greuter, D. Reuter, A. D. Wieck, M. Poggio, and R. J. Warburton, Charge noise and spin noise in a semiconductor quantum device, Nat. Phys. **9**, 570 (2013).

[26] M. J. Stanley, C. Matthiesen, J. Hansom, C. Le Gall, C. H. H. Schulte, E. Clarke, and M. Atatüre, Dynamics of a mesoscopic nuclear spin ensemble interacting with an optically driven electron spin, Phys. Rev. B **90**, 195305 (2014).

[27] A. B. Young, A. C. T. Thijssen, D. M. Beggs, P. Androvitsaneas, L. Kuipers, J. G. Rarity, S. Hughes, and R. Oulton, Polarization engineering in photonic crystal waveguides for spin-photon entanglers, Phys. Rev. Lett. **115**, 153901 (2015).

[28] E. Z. Casalengua, J. C. López Carreño, F. P. Laussy, and E. del Valle, Tuning photon statistics with coherent fields, Phys. Rev. A **101**, 063824 (2020).

[29] https://doi.org/10.5523/bris.2du6t9eh3isav2s1np371x2guo.

[30] I. Söllner, S. Mahmoodian, S. L. Hansen, L. Midolo, A. Javadi, G. Kiršanskė, T. Pregnolato, H. El-Ella, E. H. Lee, J. D. Song, S. Stobbe, and P. Lodahl, Deterministic photon–emitter coupling in chiral photonic circuits, Nat. Nanotechnol. **10**, 775 (2015).

[31] S. Ates, S. M. Ulrich, S. Reitzenstein, A. Löffler, A. Forchel, and P. Michler, Post-selected indistinguishable photons from the resonance fluorescence of a single quantum dot in a microcavity, Phys. Rev. Lett. **103**, 167402 (2009).

[32] H. J. Carmichael, *Statistical Methods in Quantum Optics 1* (Springer, Berlin, 2002).

[33] H. J. Carmichael, *Statistical Methods in Quantum Optics 2* (Springer-Verlag, Berlin, 2008).

[34] C. W. Gardiner and M. J. Collett, Input and output in damped quantum systems: Quantum stochastic differential equations and the master equation, Phys. Rev. A **31**, 3761 (1985).

[35] J. R. Johansson, P. D. Nation, and F. Nori, QuTiP 2 A Python framework for the dynamics of open quantum systems, Comp. Phys. Comm. **184**, 1234 (2013).